




Cl-Doped CdTe Crystal Growth for Medical Imaging Applications

Rubi Gul ^{1,*} , John Stuart McCloy ¹ , Magesh Murugesan ¹ , Benjamin Montag ² and Jasdeep Singh ¹¹ Institute of Materials Research, Washington State University, Pullman, WA 99164, USA² Radiation Detection Technologies, Inc., Manhattan, KS 66506, USA

* Correspondence: rubi786@yahoo.com

Abstract: CdTe:Cl doped single crystals were grown under conditions of tellurium excess by using an accelerated crucible rotation technique, modified vertical Bridgman (ACRT-MVB) method. Chlorine dopant levels were kept at 4.4×10^{19} at·cm⁻³, for all growths, while the Te excess level varied from 3.5 to 15% by weight. The relationship between the detector performance, Te inclusions, and resistivity was investigated in detail. Tellurium excess caused additional nucleation which decreased the average single crystal grain size. At the same time, the increasing Te excess level improved the electrical transport properties. In the three Cl-doped, and one In-doped CdTe crystals, detectors from Cl-doped CdTe grown under 15% Te excess showed better response to gammas and alphas, and high $\mu\tau$ for electrons (1.8×10^{-3} cm²/V), as well as for holes (5.1×10^{-4} cm²/V). The full-width half maximum for the Cl-doped CdTe were very large, as the peaks were broadened, especially at high bias. This could be due to hole trapping in a Cl-related A-center ($V_{Cd}\text{-Cl}_{Te}$)⁻, and in Cd- vacancies (V_{Cd})⁻, and electron trapping in Te-antisites (Te_{Cd})⁺.

Keywords: CdTe; radiation detector; mobility-lifetime; medical imaging; Te-inclusions

Citation: Gul, R.; McCloy, J.S.; Murugesan, M.; Montag, B.; Singh, J. Cl-Doped CdTe Crystal Growth for Medical Imaging Applications. *Crystals* **2022**, *12*, 1365. <https://doi.org/10.3390/cryst12101365>

Academic Editors: Andrey Prokofiev and Ludmila Isaenko

Received: 10 June 2022

Accepted: 22 September 2022

Published: 27 September 2022

Publisher's Note: MDPI stays neutral with regard to jurisdictional claims in published maps and institutional affiliations.



Copyright: © 2022 by the authors. Licensee MDPI, Basel, Switzerland. This article is an open access article distributed under the terms and conditions of the Creative Commons Attribution (CC BY) license (<https://creativecommons.org/licenses/by/4.0/>).

1. Introduction

The medical imaging market is growing at a compound annual growth rate of 5.8% [1]. A variety of gamma-ray and x-ray detectors, including scintillators and various semiconductor solid-state detectors, are effectively used for medical imaging. Detectors based on cadmium telluride (CdTe) and cadmium zinc telluride (CZT) have proven to be superior than the alternatives, and are already replacing scintillator-based equipment in advanced imaging modalities such as bone densitometry, oncology, dental imaging, molecular breast imaging (MBI), single photon emission computed tomography (SPECT), and hybrid SPECT/CT [2]. CdTe and CZT technology is expected to be used in the detectors of choice, if it were affordable and available, in nearly all medical imaging modalities involving ionizing radiation. CdTe has been actively investigated for more than 70 years for photovoltaics [3–6], room-temperature γ -ray and x-ray radiation detection [7–9], as well as medical imaging [10]. CdTe, due to its particular set of properties, is a good alternative to Si, CZT, and scintillators. CdTe is a II-VI chalcogenide semiconductor with a band gap of ~ 1.5 eV at room temperature, which can be relatively easily doped as *p*- or *n*-type. It has high stability (formation enthalpy ~ 100 kJ mol⁻¹), high absorption coefficient ($>5 \times 10^5$ cm⁻¹), and near optimum band gap for visible absorption. Its better intrinsic hole-transport properties [11], compared to CZT [12,13], make CdTe a strong candidate for applications where stability under very high count-rates is needed.

Even after two decades of research, CdTe and its alloys remain the desired choice for room-temperature radiation detection, but its widespread use is limited by high-cost due to the low yield and long production times. The limiting factors for the single crystal yield include: high melt-to-solid thermal conductivity ratio, the low thermal conductivity of solid phase, symmetry of the crystal structure, and clustering in the melt [14]. To improve the yield and performance, several growth techniques, including traveling heater method (THM), high pressure Bridgman (HPB), vertical Bridgman (VB), and modified vertical

Bridgman (MVB) have been attempted [15,16]. The addition of the accelerated crucible rotation technique (ACRT) to MVB has been effective in achieving many desirable aspects, including improved quality of the crystal, shorter growth time, stable growth interface, lower tellurium-rich secondary phases, increased uniformity, and highly achieved stoichiometry [17–21]. THM growth rate is ~1–3 mm per day, whereas growth by ACRT-MVB is ~1–2 mm per hour. Despite being grown at very slow rates, crystals grown by THM have a high-volume of Te-rich secondary phase [22] which require post-growth annealing [23].

In the current work, CdTe growth, doped with Cl for application to medical imaging, is studied. The excess Te during the growth is varied, which has both positive and negative effects. Excess Te causes a cooling effect [24], resulting in more nucleation sites, lowered grain size, and lower crystal quality. However, Te excess does reduce the Cd-related defects, especially V_{Cd} induced during the lower partial pressure of Cd during the melt growth [25]. Te-excess improves the charge carrier's lifetime and mobility, which improves the detectors spectroscopic performance [24,26,27]. The distinctive electrical transport property for CdTe:Cl is the dominant hole mobility which is related to the Cl-related A-center ($Cl_{Te}-V_{Cd}$) [28]. In addition, Cl as a dopant cause an increase in the resistivity, and compared to other dopants, it generated only a shallow donor which has negligible contribution to the lifetime [29,30].

2. Experimental Procedures

2.1. Crystal Growth

CdTe crystals, including one CdTe:In having $8.8 \times 10^{16} \text{ at}\cdot\text{cm}^{-3}$ In with 3.5% excess Te, and three CdTe:Cl with $4.4 \times 10^{19} \text{ at}\cdot\text{cm}^{-3}$ Cl, under various Te excess conditions 3.5, 7.5% and 15%, were grown by using a 43-zone ACRT-MVB, 4 inch electrodynamic gradient freeze (EDG) furnace. The pBN crucible and fused-quartz ampoule were etched with aqua-regia solution and 20% hydrofluoric acid solution, respectively. About 1 kg CdTe-charge was prepared in a glove-bag. The 63 mm inner diameter (ID) pBN crucible, with the CdTe-charge was sealed in a 69 mm (ID) quartz ampoule, under a 10^{-8} torr vacuum by using 5-rotary torches. In all growths, the superheating temperature was kept ~50 K above the melting point, which varies with the excess percentage tellurium. The temperature gradient was kept at 50 K/inch, and the cooling rate at 4 K/h between 1273–973 K and at 35 K from 973 K to the room temperature. Growth rates of 1 mm/h and 2 mm/h were employed for Cl and In doped crystals, respectively. The concave interface was observed in all the crystal growth and can be seen clearly in Figure 1c. Further details of the growths are provided in Table 1.

Table 1. Growth description for all CdTe crystal growths.

No	Crystal Growth	Dopant (cm^{-3})	Te _{ex} (wt.%)	Te _{ex} (cm^{-3})	pBN	ACRT
1	CG224 (CRY-1)	In: 8.8×10^{16}	3.5	9.2×10^{20}	Y	Y
2	CG241 (CRY-2)		3.5	9.2×10^{20}	Y	Y
3	CG235 (CRY-3)	Cl: 4.4×10^{19}	7.5	2.2×10^{21}	Y	Y
4	CG247 (CRY-4)		15.0	4.8×10^{21}	N	Y

CRY-1, the CdTe:In was grown as a reference crystal for three CdTe:Cl growths. Te excess was achieved with a total of 36.27 g of Te. The crystal growth time was 11.8 days with a growth rate of 1 mm/h. The ingot and wafers, with highlighted grain-boundaries are shown in Figure 1a. Ingots had a few big grains with an abundance of twins.

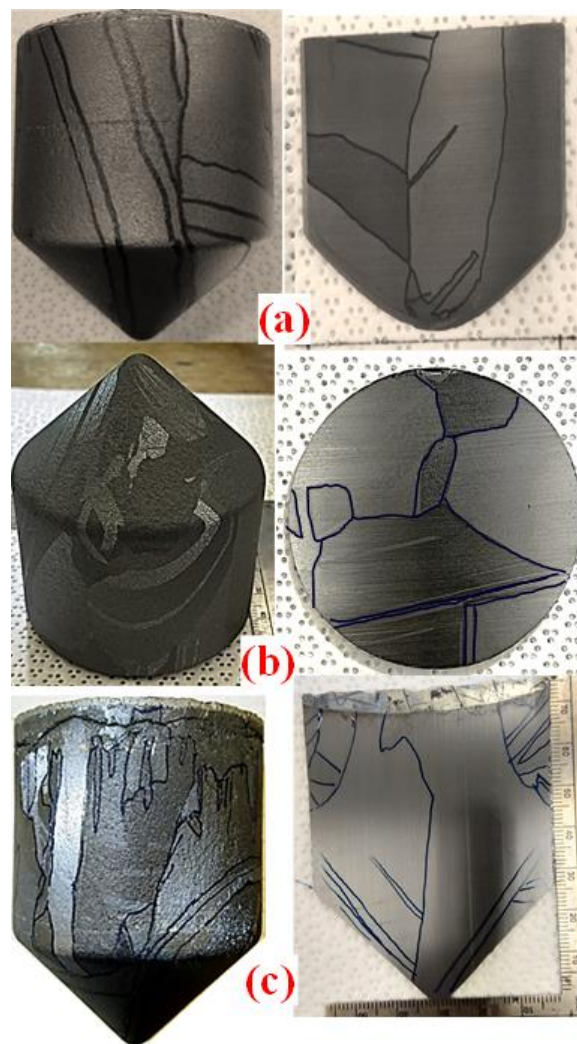


Figure 1. Pictures for ingots and marked wafers from (a) CRY-1, (b) CRY-2, and (c) CRY-3 growths.

In Cl-doped CdTe crystal growths, the Cl level was kept constant at $4.4 \times 10^{19} \text{ at}\cdot\text{cm}^{-3}$. CRY-2 was grown with the lowest Te excess of 3.5%. The grown ingot and wafer cuts with marked grain boundaries are shown in Figure 1b. After cutting the tip and heel region, the bulk region was further cut into axial wafers. Crystals had big grains, and fewer twins and sub-grain boundaries.

The third growth, CRY-3, was accomplished with 7.5% by weight of excess Te. The grown ingots and wafers with marked grain boundaries are shown in Figure 1c. The ingot had large grains with few twins and subgrain boundaries.

CRY-4 was the last growth with the highest excess Te of 15% by weight. The crystal growth was performed with 2 mm/h rate, 2 times faster than other three growths. The ingot had a high accumulated Te region at the heel region, as well as the ingot surface, as shown in Figure 2. The grains were small in size with abundant subgrain boundaries.

Ingots were sand blasted to clean off growth contamination and excess Te at the surfaces. Roughly 2–3 mm wafers with high Te accumulated region were cut from the heel side. Ingots were cut into ~2–3 mm thick axial and radial wafers by using a programmed wire saw. Wafers were marked for the single crystals and were further cut into $\sim 10 \times 10 \times 2 \text{ mm}^3$ small wafers. Small wafers were 6-sides polished with $1 \mu\text{m}$ and $0.05 \mu\text{m}$ Al_2O_3 particles. Detectors were fabricated by sputtering $\sim 50 \text{ nm}$ Au contacts on two planar surfaces using a plasma chamber. To reduce the leakage current, a few samples before Au sputtering were etched for 1–2 min with 1–2% bromine methanol solution.

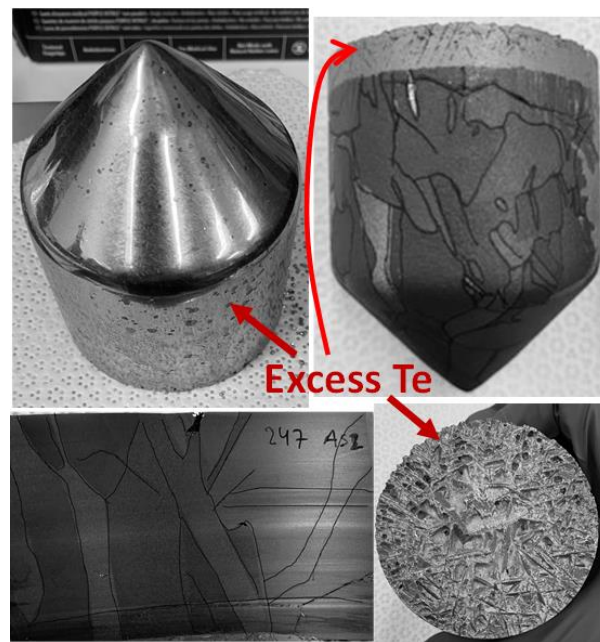


Figure 2. Pictures of the CRY-4 ingot showing Te accumulation at the heel and at the surface of the ingot and the axial wafer from the bulk region with marked small grains.

2.2. Characterizations

To test the materials' quality and detectors' performance, different characterizations were employed. Electrical properties were measured by using current/voltage (I/V) characteristic plots. The setup includes a planar geometry configuration (parallel plate configuration) using a Keithley 6105 resistivity adaptor in combination with a Keithley 237 high voltage power supply.

To evaluate the Te-rich secondary phases, their size, volumes and densities, infrared (IR) microscopy was performed on wafers from different locations in the ingot. The statistical inclusions distribution was performed by using Image Pro Plus software. An 830 nm illumination light was used to study the Te phases. 2–5 samples from each growth were analyzed to quantify Te-rich secondary phases. The scanned area in XY-plan was kept $5 \times 5 \text{ mm}^2$, with 10×10 frames within a 0.5 mm thickness along Z-axis.

The detector performance was tested by using γ -ray spectroscopy. The charge transport properties, as defined by the mobility life-time product, i.e., $\mu\tau$ -product, was determined by fitting the Hecht equation. In γ -ray spectroscopy, the charge induced due to the radiations is measured by the feedback capacitor in the charge sensitive preamplifier that converts the current from the drift of charge carriers inside the detector to a proportional voltage pulse. Signal is further enhanced by an amplifier and then passed through a series of pulse-shaping circuits. The signal is then passed through a set of ADC (analog to digital converter) and MCA (multi-channel analyzer) circuits. Plotting the channel vs. number of pulses in each channel generates a pulse height spectrum which is used to determine the peak positions for a given irradiation source and applied electric field. The field dependence of the peak position can be fit into the following modified Hitch equation, where the hole contribution is ignored in the total signal,

$$Q/Q_0 = \lambda_e D^{-1}(1 - \exp(-D/\lambda_e)) + Bg$$

Here, Q is the charge collected by the detector, Q_0 the charge generated by the incident radiation, D is the detector thickness, λ_e is the electron drift length and is equal to $\mu\tau E$. Bg is the system background which is roughly $-(20-50)$.

To test the CdTe:Cl detectors for the high flux applications, an experiment was designed and performed with an ^{241}Am source with activity of 4.8 Ci in the TRIGA Mark II

nuclear reactor facility at Kansas State University. The target was to achieve 500,000 counts per second (cps)/mm². Details are reported in Section 3.5.

3. Results and Discussion

3.1. Crystal Quality

During the melt growth, different types of extended defects such as the subgrain boundaries, twins, and Te secondary phases are induced in the crystals [31]. The crystal quality varies with the Te excess during the crystal growths. The studies show that increasing Te excess cause a decrease in the melting point (liquidus), while at the same time, it reduces the solid CdTe region due to the retrograde solidus character. Thus, Te excess in the melt-solution meets a smaller deviation from stoichiometry [32]. The grains are becoming smaller with the increasing Te excess due to more nucleation [24]. Comparing CRY-1 and CRY-2, In-doped versus Cl-doped crystals (Figure 1), the latter has slightly larger grains and better crystal quality with fewer twins. In Cl-doped growths, it is clear that the 3.5% excess Te growth has a superior quality; the crystallinity is better with fewer twins and larger grains. This indicates that Te excess enhances the nucleation causing subgrain boundaries and smaller grains.

3.2. IR Spectroscopy

In CdTe, Te inclusions are generated from the non-stoichiometric melt growth. In addition, the excess Te during the growth affects the flux of inclusions [33]. The density and the size of the Te inclusions drastically affect the detector performance. Te inclusions > 10 μm with a density ~10⁵ cm⁻³ or greater degrade the detector performance [34–36].

The IR images and the inclusion data for each growth are shown in Figures 3–6. In CRY-1, CdTe:In, a 3.5% excess Te induced large inclusions (Figure 3). In all three CdTe:Cl growths, the densities of inclusions remain roughly 1–8 × 10⁵ cm⁻³. On the other hand, the mean size of Te inclusions with the increased level of Te in the melt decreases from micrometer to nanometer level. In the case of CRY-4, due to the higher growth rate, some Te remained undissolved and migrated towards the heel during the solidification of the crystal. Inclusion average size and density is comparatively low in Cl-doped crystals. The excess Te induces electrically inactive traps (Te_{Cd}⁰) and some Cl-related A-centers (Cl_{Te}-V_{Cd})⁻. The Cl related traps, A-centers and Cl antisites [Cl_{Te}]⁺ are reported as the most stable and dominant traps with a low formation energy ~0.12 eV [37,38]. These traps are causing a *p*-type conductivity in CdTe:Cl crystals [39].

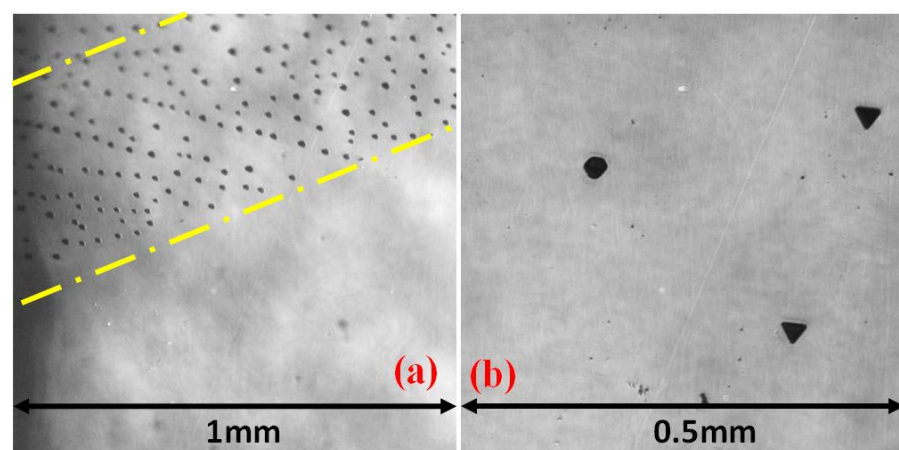


Figure 3. IR microscopy data for CRY-1 sample; (a) Te decoration on a dislocation side. (b) Large prismatic and triangular inclusions.

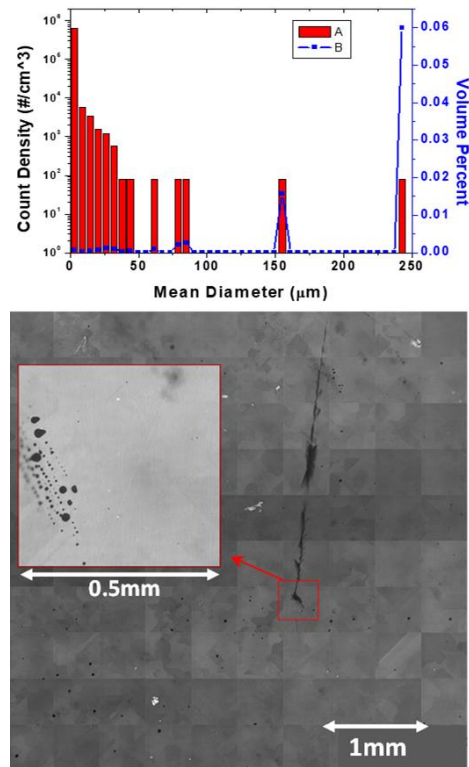


Figure 4. CRY-2, $5 \times 5 \text{ mm}^2$ sample; **(top)** Te inclusions with average density $\sim 6.4 \times 10^5 \text{ cm}^{-3}$ and size $\sim 1.2 \text{ }\mu\text{m}$. **(bottom)** 2D-IR image, Te decorated twins in tiled images of the sample. Inset showing the triangular defects and alignment of the inclusions.

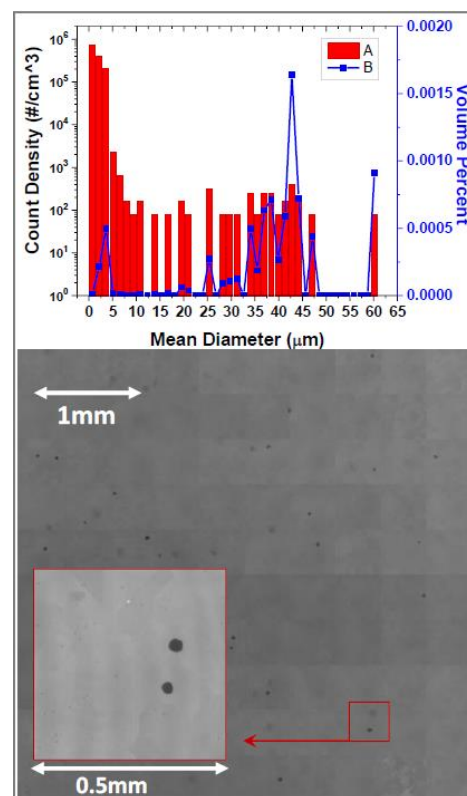


Figure 5. CRY-3, $5 \times 5 \text{ mm}^2$ sample; **(top)** Te inclusions with average density $\sim 1.3 \times 10^5 \text{ cm}^{-3}$ and size $\sim 1.6 \text{ }\mu\text{m}$. **(bottom)** 2d-IR image with an inset showing 2 large inclusions.

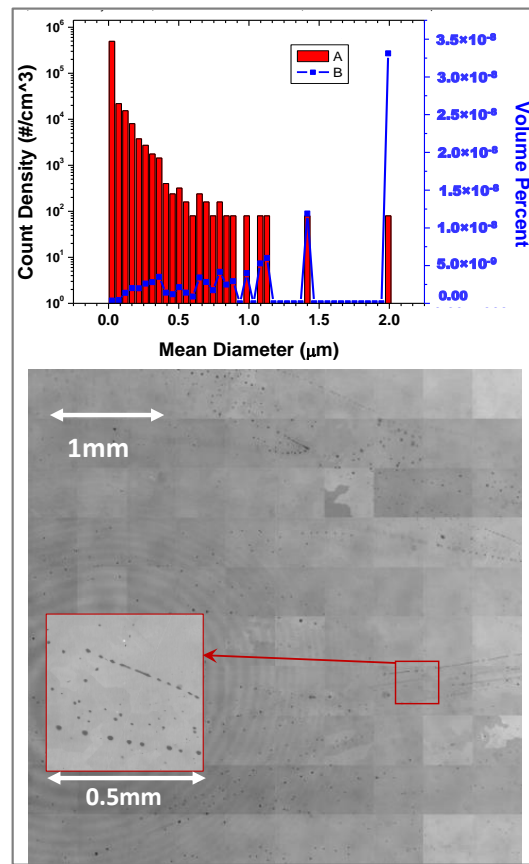


Figure 6. CRY-4, a 5 × 5 mm², multi grain sample; (top) Te inclusions with average density ~5.5 × 10⁵ cm⁻³ and size ~0.02 μm. (bottom) 2d-IR image with an inset showing inclusions’ alignment.

Another reason for decreased IR detected density and size of Te inclusions, as determined by the IR data shown in Figures 3–7, may be due to the Te incorporation to its stoichiometric positions causing the dissociation of A-centers and Cl_{Te}⁺ trap. In addition, when there is a probability of In addition, there is a probability for the formation of Te_{Cd}⁺. These new states of point defects may change the nature of CdTe:Cl from *p*-type to *n*-type. The role of point defects in the electrical properties of CdTe:Cl crystals need to be investigated in the future.

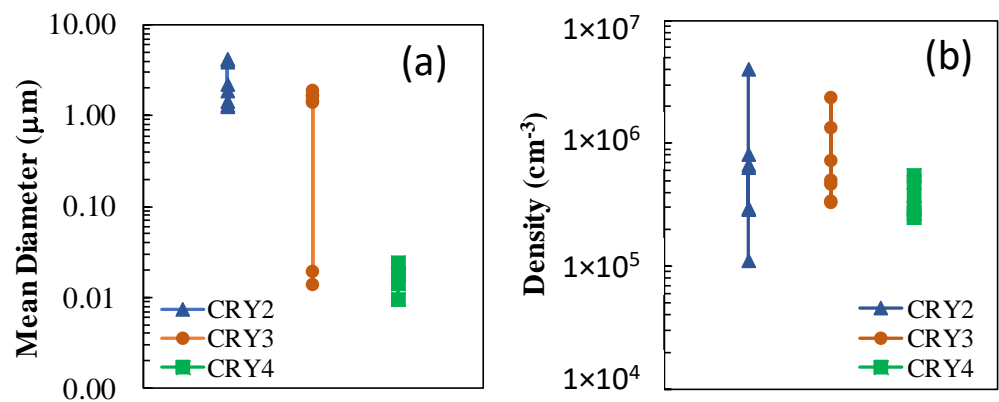


Figure 7. Te inclusions, (a) size and (b) density for samples from different positions in CdTe:Cl ingots.

A comparison plot for Cl-doped samples shown in Figure 7 indicates that the average size and density of Te inclusions is slightly decreasing with the increasing weight % of

excess Te. There is a high probability for Te to compensate the Cd vacancies by forming more Te_{Cd}^+ or the dissociations of Cl_{Te}^+ and A-center, as mentioned before.

Different isothermal and gradient annealing treatments have been effectively employed to reduce the Te inclusions [40–42]. Besides single step annealing, 2-step heat treatments involving Cd- and Te-annealing have been successfully used to eliminate the inclusions as well as to recover the resistivity of the crystals [43,44]. To study the isothermal-annealing effects on inclusions in CdTe:Cl crystals, Cd annealing experiments were performed at 750 °C for 12 h. The size and the density of inclusions decreases after annealing, as shown in IR images in Figure 8 and summary plots in Figure 9. The change in inclusions is probably due to the change in Te-related point defects, as well as the thermal migration of inclusions towards the surface of the samples. The deep trap Te_{Cd}^+ , which mainly caused the high resistivity is compensated by Cd, as a result the resistivity decreases. In addition, the Cd annealing causes a decrease in Cd vacancies and an increase in Cd interstitials, overall causing a decrease in resistivity. The Cl-induced trap, Cl_{Te}^+ still remains dominant over other traps. During the annealing, metallic impurities originally gettered in Te inclusions are detrapped. An adverse consequence of Cd annealing is due to the abovementioned rearrangements of point defects, resulting in a significant deterioration of the resistivity, roughly 2–4 orders of magnitude. The attempt to measure the spectral response of the annealed detectors failed due to the low resistivity, high dark current, and low signal to noise ratio. During the annealing some big triangular inclusions, due to the so-called dislocation-loop punching mechanism, were identified [45]. These defects are probably induced due to the exothermic reaction of the elemental Te within the inclusions with the diffused Cd atoms. This generates heat and pressure in the CdTe matrix, causing distortions and movements around inclusions and the dislocations.

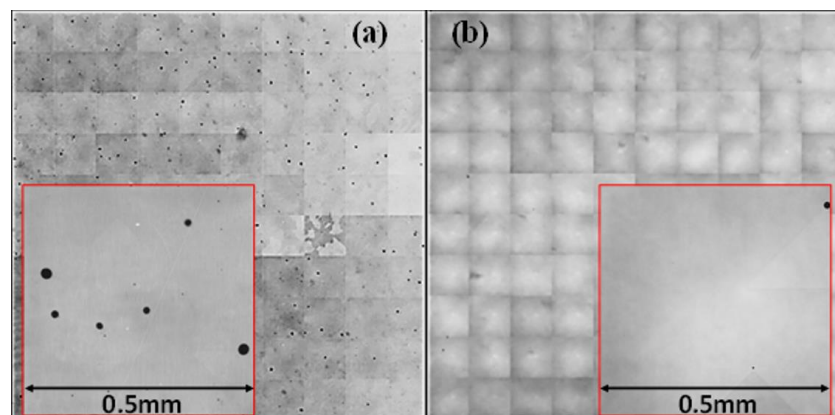


Figure 8. IR images for CRY-3, $5 \times 5 \text{ mm}^2$ wafer, (a) as grown with big inclusions and (b) Wafer after the annealing. Insets show a $0.5 \times 0.5 \text{ mm}^2$ area, where big inclusions in (b) are annealed out.

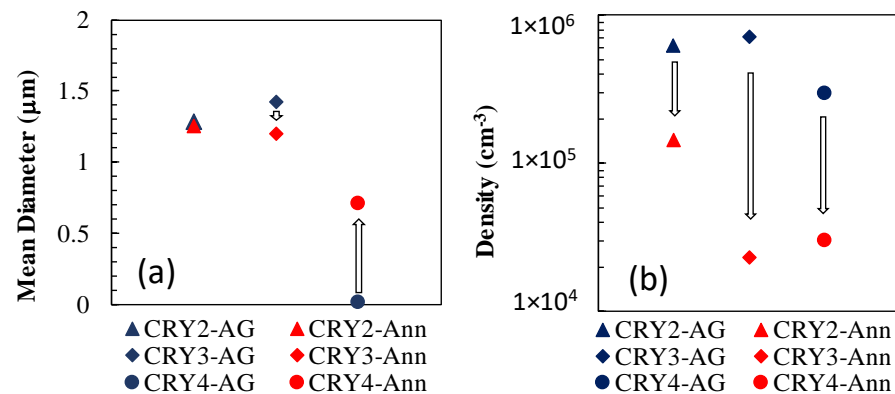


Figure 9. A comparison of Te inclusions; (a) size, and (b) density, for CdTe:Cl as-grown (AG) and after annealing at 750 °C for 12 h (Ann).

3.3. Electrical Characterizations

Two to five detectors from different growth positions are tested for bulk resistivity by measuring I/V characteristic plots. The results from I/V characteristic plots for In and Cl doped crystals grown under 3.5% excess Te are shown in Figure 10. The average values of resistivity are provided in Table 2.

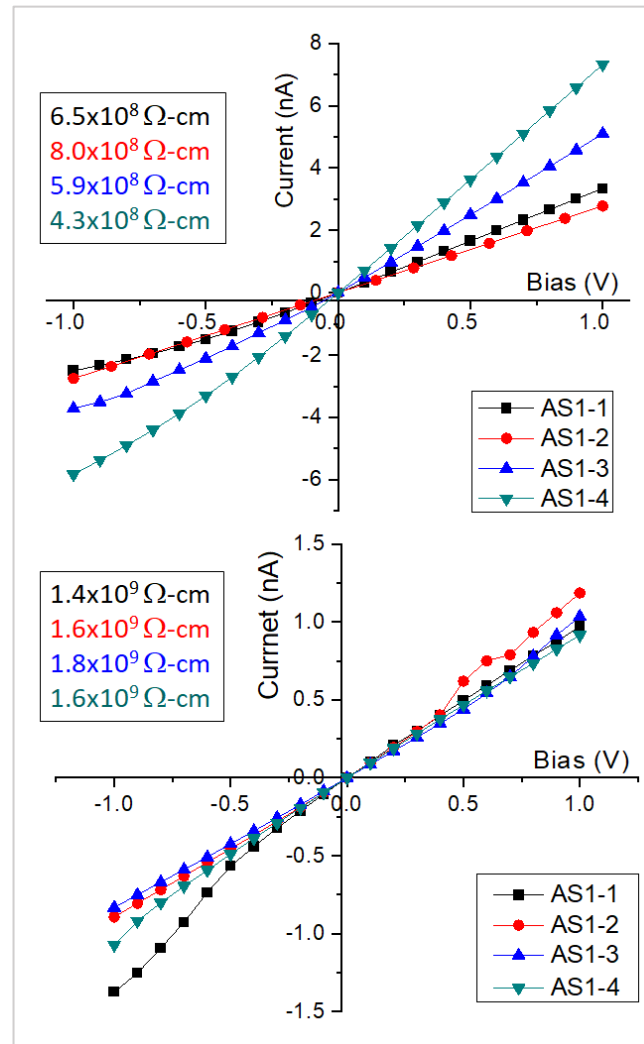


Figure 10. I/V plots for the CRY-1 and CRY-2 central axial wafers (AS1), tested at different locations along the growth directions. The CRY-1 (top) samples had the lowest average resistivity $\sim 6 \times 10^8 \Omega\text{-cm}$, while CRY-2 (bottom) had $\sim 5 \times 10^9 \Omega\text{-cm}$, the highest amongst the four growths.

The CRY-1 resistivity, as shown in Figure 10, is the lowest amongst the group. It indicates that at 3.5% Te-excess, combined with In doping, was unable to achieve the high resistivity ($\sim 10^{10} \Omega\text{-cm}$), a prerequisite for a room temperature radiation detectors. The average resistivity for the CRY-2 crystals was $\sim 5 \times 10^9 \Omega\text{-cm}$, the highest amongst the group.

In CRY-3 crystals, a central wafer was analyzed for resistivity at different positions with a focus on the surface preparation of the detectors before contacts fabrication. Data indicates that resistivity increases slightly along the growth direction, which is due to the increasing Te concentration along the growth direction. In addition, the surface etching is not making any improvement. Resistivity in wafer is increasing from $0.6\text{--}1.9 \times 10^9 \Omega\text{-cm}$, for detectors polished and etched with 1% Br-methanol solution for 1 min and hydrogen peroxide for 5 min.

Table 2. Summary of results for CdTe:Cl growths. N_t is volumetric density, OD is outer diameter.

Quality Parameters	CRY-1	CRY-2	CRY-3	CRY-4
	3.5% Te-Excess	3.5% Te-Excess	7.5% Te-Excess	15% Te-Excess
Crystal Quality— Te inclusion Size/Density	Prismatic defects and Big inclusions	$N_t: (1.1\text{--}8.0) \times 10^5 \text{ cm}^{-3}$ OD: 1.2–4.0 mm Big inclusions	$N_t: (3.3\text{--}7.2) \times 10^5 \text{ cm}^{-3}$ OD: 0.01–1.6 mm Medium inclusions	$N_t: (2.5\text{--}5.5) \times 10^5 \text{ cm}^{-3}$ OD: 0.01–0.02 mm Small inclusions
Resistivity: ($\Omega\text{-cm}$)	$(4\text{--}8) \times 10^8$	$\sim 1.6 \times 10^9$	$(0.6\text{--}2) \times 10^9$	$(1\text{--}5) \times 10^9$
$\mu\tau_e$ -product (cm^2/V)	$(0.09\text{--}0.1) \times 10^{-4}$	$(0.2\text{--}0.4) \times 10^{-3}$	$(0.3\text{--}1.1) \times 10^{-3}$	$(0.5\text{--}1.8) \times 10^{-3}$
$\mu\tau_h$ -product (cm^2/V)		$(1.04\text{--}1.80) \times 10^{-4}$	$(1.04\text{--}1.80) \times 10^{-4}$	$(0.25\text{--}1.3) \times 10^{-3}$
Average value	~ 0	$\sim 1.33 \times 10^{-4}$	$\sim 2.2 \times 10^{-4}$	$\sim 5.12 \times 10^{-4}$

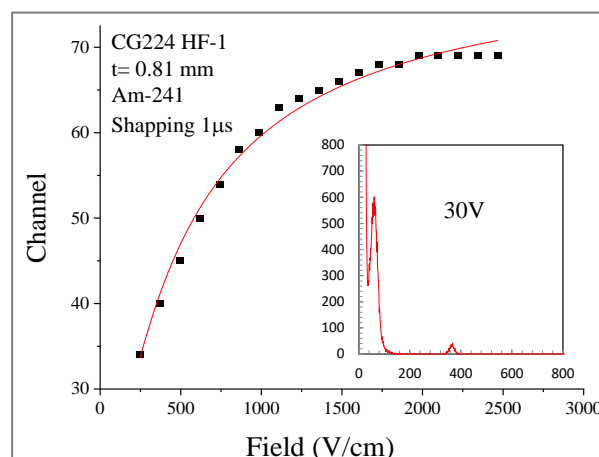
The CRY-4 wafer was tested at 3 different locations. The crystal exhibits similar behavior of increasing resistivity along the growth direction, as observed in previous growths. The average value of resistivity determined from I/V plots is $\sim 3 \times 10^9 \Omega\text{-cm}$.

Comparing the data for all Cl-doped detectors, the average resistivity is $\sim 10^9 \Omega\text{-cm}$, and a slight increase in the value due to the increasing Te excess. Cl-doping causes generation of Cl_{Te}^+ , a shallow donor or the dominant Cl-related A-center which makes the CdTe:Cl *p*-type [46–48]. Lindström et al. [39] related it with the self-compensation and self-purification due to Cl doping.

3.4. Detector Performance

The gamma-ray response and the $\mu\tau$ product, as determined by Hecht equation fitting, was measured by using ^{241}Am and ^{57}Co standard sources as well as a 5 MeV ^{241}Am - α source. Multiple, 1–2 mm thick detectors were selected from different axial and radial locations within the ingots. Radiation response measurements were attempted for the Cd annealed CdTe:Cl detectors but failed, most probably due to an increased conductivity as well as the high leakage current; these samples showed no response to ^{241}Am standard source.

The ^{57}Co source was used to test the response as well as the $\mu\tau$ product for CRY-1, as shown in Figure 11. The calculated $\mu\tau$ value was $1 \times 10^{-4} \text{ cm}^2/\text{V}$ which is the lowest amongst the four growths.

**Figure 11.** $\mu\tau_e$ -measurements ($1.0 \times 10^{-4} \text{ cm}^2/\text{V}$) and gamma response to ^{241}Am for CRY-1.

All Cl-doped detectors were tested by ^{241}Am , and Am- α source for $\mu\tau_e$ and $\mu\tau_h$ measurements, respectively. CRY-2 and CRY-3 detectors response were similar with roughly $2.8 \times 10^{-4} \text{ cm}^2/\text{V}$ $\mu\tau_e$ values, as shown in Figures 12 and 13. The detectors from CRY-4, with highest Te excess had highest $\mu\tau$ value of $2.8 \times 10^{-3} \text{ cm}^2/\text{V}$, see Figure 14. Comparing the $\mu\tau_e$ values for In- and Cl-doped CdTe detectors, with 3.5 excess Te, the lat-

ter has the higher $\mu\tau$. Similarly, comparison of three Cl-doped CdTe detectors showed that the 15% excess Te (Figure 14) achieved the highest $\mu\tau$ -product, making it the best detector performance.

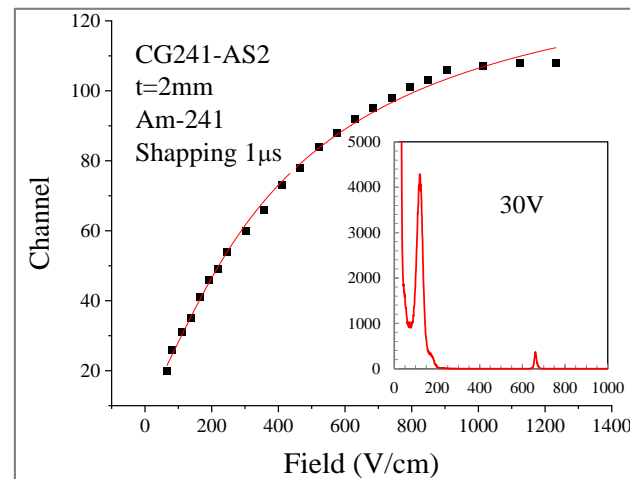


Figure 12. $\mu\tau_e$ measurements ($2.9 \times 10^{-4} \text{ cm}^2/\text{V}$) and gamma response to ^{241}Am for CRY-2.

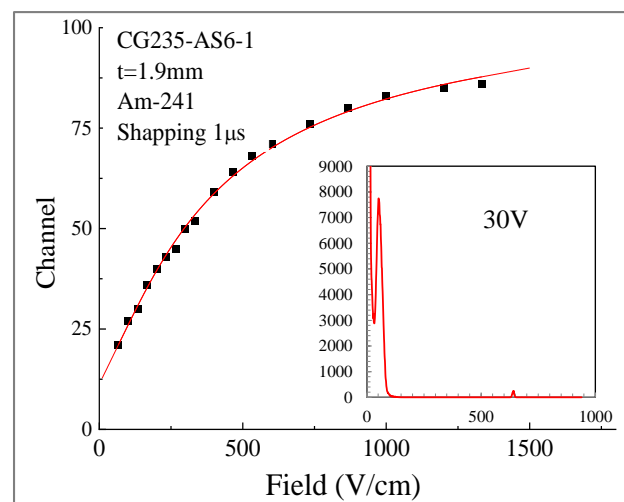


Figure 13. $\mu\tau_e$ measurements ($\sim 2.9 \times 10^{-4} \text{ cm}^2/\text{V}$) and gamma response to ^{241}Am for CRY-3.

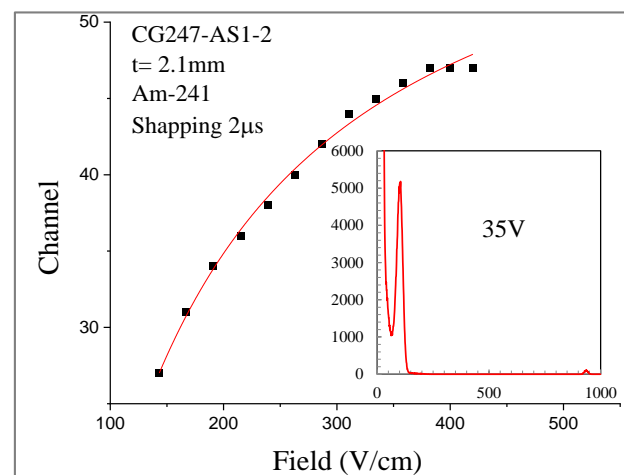


Figure 14. $\mu\tau_e$ measurements ($\sim 1.3 \times 10^{-3} \text{ cm}^2/\text{V}$) and gamma response to ^{241}Am for CRY-4.

In CdTe:Cl, an interesting behavior of the detectors towards the increasing bias was observed; increasing the bias degrades the peak discrimination due to the so called polarization [49]. Generally, this is not the case with CZT detectors. A comparison of bias dependence of photopeak of ^{57}Co source measured by CRY-3 and one of the CZT:In detector, both growth were at 7.5% of Te-excess, is shown in Figure 15. The full width at half-maximum (FWHM) values increased due to the peak broadening. This behavior is attributed to the hole and electron trapping, by Cd vacancies and Te antisites, respectively [26].

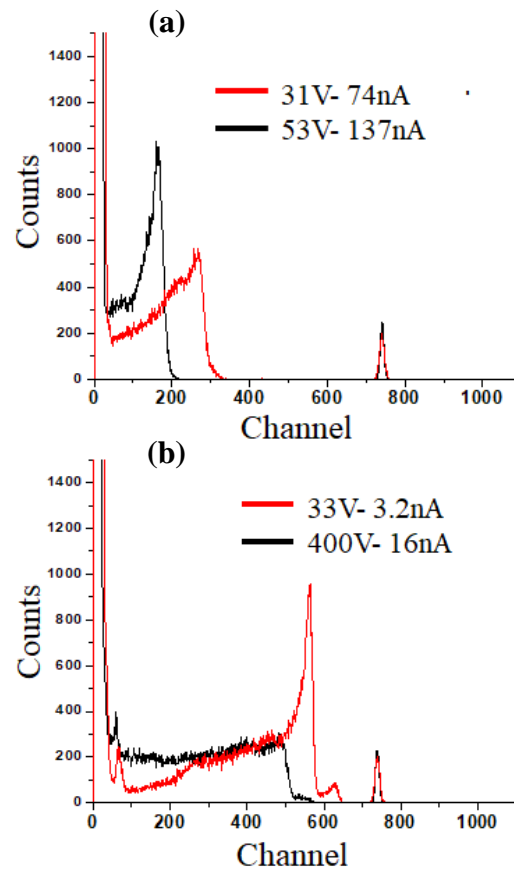


Figure 15. Bias dependence of ^{57}Co photopeak, measured by: (a) CdTe:Cl (1.9 mm) and (b) CZT:In (1.4 mm) detector with 7.5% Te-excess growths.

An ^{241}Am α source was used to determine the $\mu\tau_h$ and the response of detectors towards α radiation. The average $\mu\tau_h$ values have an increasing trend, like $\mu\tau_e$ with the increasing Te excess, see Table 2. The results for CRY-4 are shown in Figure 16. At the highest bias of 550 V, the peak shape was broadened, but the signal was still good due to high charge collection efficiency of the detector. At 550 V the leakage current reached to $\sim 0.74 \mu\text{A}$. As compared to $\mu\tau_e$, much higher biases up to 550 V were applied without significant distortion in $\mu\tau_h$ measurements.

A group of detectors were tested for $\mu\tau_e$ and $\mu\tau_h$ with a focus on surface preparation effects, before the Au sputtering. Good response and high $\mu\tau_e$ was observed for the detectors polished and etched before the Au sputtering, Figure 17. On the other hand, good radiation response and good $\mu\tau_h$ was observed for the detectors with polished only surfaces, Figure 18. This difference in collection of holes/electrons for different contact configurations was observed in γ -ray spectra as well.

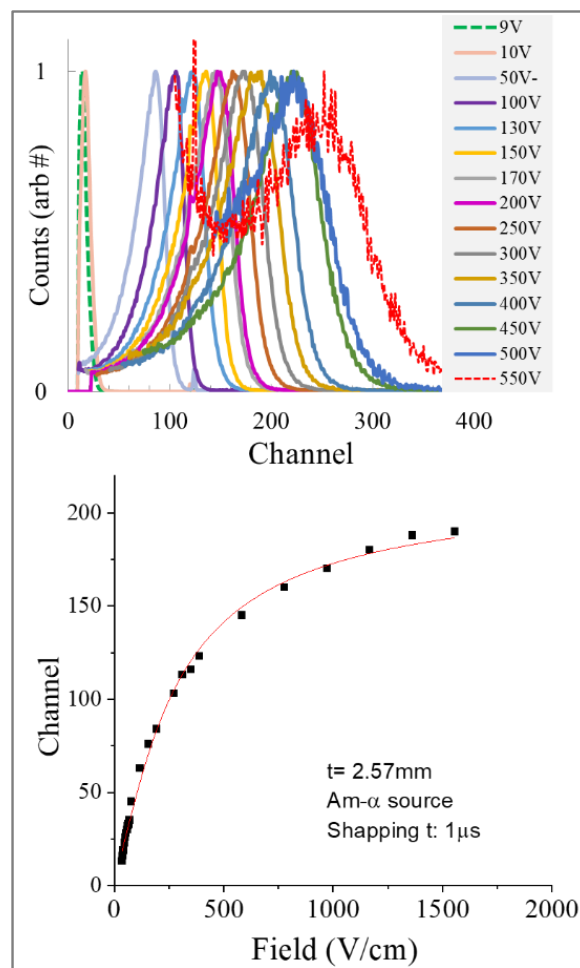


Figure 16. Spectral response at increasing applied bias, and Hecht equation fitting for $\mu\tau_h$ measurements ($5.6 \times 10^{-4} \text{ cm}^2/\text{V}$) by using ^{241}Am α source for CRY-4.

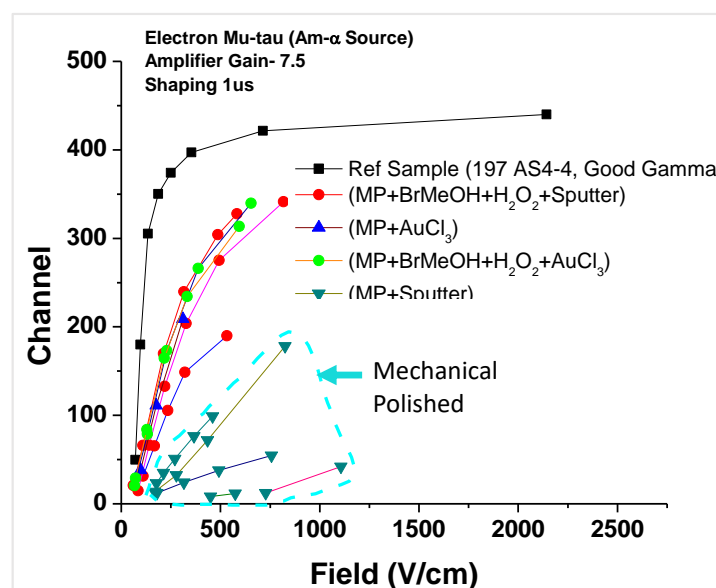


Figure 17. $\mu\tau_e$ products determined by using ^{241}Am -source for different treated surfaces in CRY-3 detectors.

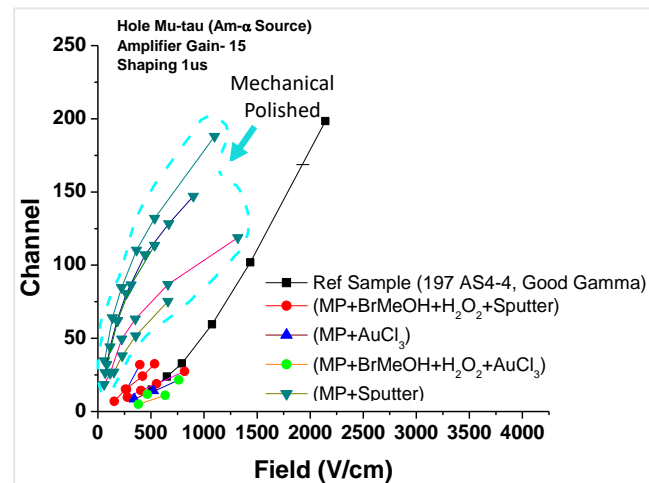


Figure 18. $\mu\tau_h$ products determined by using ^{241}Am - α source for different treated surfaces in CRY-3 detectors.

The $\mu\tau$ products, the excess Te during the crystal growth, and the induced Te inclusions are analyzed together, in Table 2. It is obvious from the data that the size of the inclusions is anticorrelated with the $\mu\tau$ product of the devices. The greater the size of the inclusions, the more the degradation of the detector performance [23]. The dependence of $\mu\tau_e$ and $\mu\tau_h$ products on the excess Te conditions is shown in Figure 19. The $\mu\tau$ values for electron as well as for holes increase with the excess Te. The comparison of these results indicates that the highest level of the Te excess, achieved better $\mu\tau_h$ and $\mu\tau_e$ products $\sim 5.1 \times 10^{-4} \text{ cm}^2/\text{V}$ and $2 \times 10^{-3} \text{ cm}^2/\text{V}$, respectively.

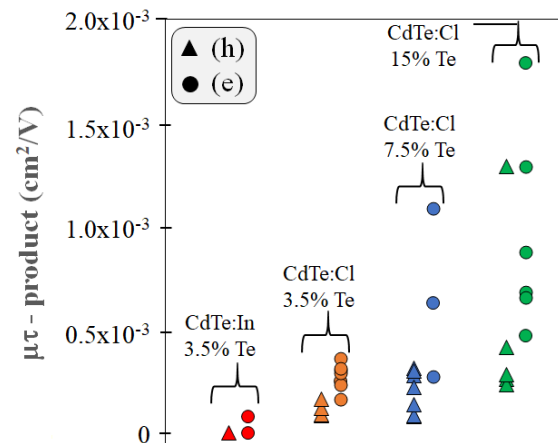


Figure 19. A summary of $\mu\tau$ products for holes and electrons in relation with Te-secondary phases, showing roughly a linear relationship with the averaged $\mu\tau$ values.

3.5. High Flux Measurements

A high-count rate experiment was designed and performed for the CdTe-Cl doped detectors. To achieve 500,000 counts per second (cps)/ mm^2 , an ^{241}Am source with activity of 4.8 Ci was placed 10 inches from the detector. The experiment was prepared in the reactor bay of the TRIGA Mark II nuclear reactor facility at Kansas State University. The high-count rate electronics package was equipped with a CRY-3 material, $4.12 \times 5.01 \text{ mm}^2$ detector. The package was mounted inside the Rad-Source 1800 X-ray generator. The detector was biased at 500 V and was irradiated with 160 keV, 12 mA X-ray generator power with 16 km zinc, 80.5 km of aluminum attenuation. Ten minute measurements were collected. A count rate on the order of 2.5 million cps ($\sim 100,000 \text{ cps}/\text{mm}^2$) was achieved. Overall system configuration measured 500,000 cps/ mm^2 count rate successfully. The modeled X-ray

flux at the device as a function of generator power showing linear output with power, as expected and the measured flux by CRY-3 in cps/mm² are shown in Figure 20. It is clearly observed that the detector begins to suffer from dead time at approximate 3 mA generator power and suffers from paralyzation, where the detector went “off” due to dead time and thus reducing the measured count rate was observed. A count rate of 110,000 cps/mm² was measured before paralyzation, as shown in the linear curve. The measurements performed on this single pixel device demonstrated the capability for the Cl-doped CdTe detectors for high-count rate applications in medical imaging devices.

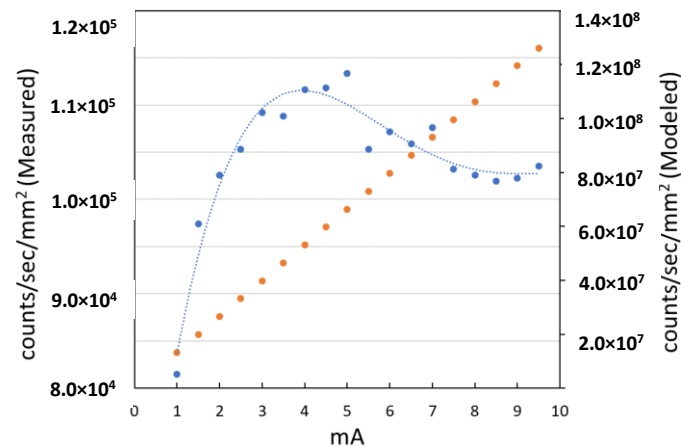


Figure 20. The measured high count rate (blue) by a 4.12×5.01 mm² CdTe:Cl detector (CRY-3), and modeled count rates (orange) for the X-ray power-generator for the high count-rate measurements.

4. Conclusions

The comparison of the crystal quality, electrical properties, and response towards the radiation demonstrates that the growth from off-stoichiometric melts with high excess Te produced high performance crystals. It was observed that ACRT-MVB grown crystals have high performance, with charge carrier mobility-lifetime, $\mu\tau_h$ was measured at 5.3×10^{-4} cm²/V and the $\mu\tau_e$ was measured at 1.8×10^{-3} cm²/V. These values compare favorably with THM-grown CdTe/CZT material in literatures. The results for the high excess Te indicate that although the crystallinity of the ingots, especially the size of the grains, decreases, at the same time the detectors' performance improved. Comparison of In- and Cl-doped CdTe detectors with same excess Te growths indicates that $\mu\tau$ product for CdTe:Cl is better than CdTe:In. In addition, due to a Cl-related acceptor level, the $\mu\tau_h$ is dominant. The high count-rate measurements demonstrate the capability of Cl-doped CdTe for high-count rate applications in medical imaging devices. This is a major achievement providing evidence that the ACRT method is appropriate to produce CdTe for high-count rate applications such as those in medical imaging.

Author Contributions: Conceptualization, R.G.; methodology, M.M. and J.S., formal analysis, R.G., investigation, R.G.; writing—review and editing, R.G.; project administration, J.S.M.; funding acquisition, B.M.; All authors have read and agreed to the published version of the manuscript.

Funding: The work was supported by the National Institutes of Health, under award number 1R41EB029280-01 for a Small Business Technology Transfer (STTR). Project entitled “The Rapid-Production of the High-Performance and Affordable Cadmium Telluride and Cadmium Zinc Telluride for Medical Imaging Applications”.

Data Availability Statement: The data presented in this study are available on reasonable request from the corresponding author.

Acknowledgments: The authors thank Santosh Swain and Saketh Kakkireni for helpful comments and related work.

Conflicts of Interest: The authors declare no conflict of interest.

References

1. Laura Wood, S.P.M. *Global Medical Imaging Market Forecast to 2024 with Siemens, GE Healthcare, Philips, Toshiba Medical, Hitachi Medical & Fujifilm Holdings Dominating*; Research and Markets: Dublin, Ireland, 2019.
2. Hruskaa, C.B.; O'Connora, M.K. Nuclear imaging of the breast: Translating achievements in instrumentation into clinical use. *Med Phys.* **2013**, *40*, 050901. [[CrossRef](#)] [[PubMed](#)]
3. Loferski, J.J. Theoretical Considerations Governing the Choice of the Optimum Semiconductor for Photovoltaic Solar Energy Conversion. *J. Appl. Phys.* **1956**, *27*, 777–784. [[CrossRef](#)]
4. Green, M.A. Third generation photovoltaics: Ultra-high conversion efficiency at low cost. *Prog. Photovolt. Res. Appl.* **2001**, *9*, 123–135. [[CrossRef](#)]
5. Bosio, A.; Rosa, G.; Romeo, N. Past, present and future of the thin film CdTe/CdS solar cells. *Sol. Energy* **2018**, *175*, 31–43. [[CrossRef](#)]
6. Chander, S.; Dhaka, M. CdCl₂ treatment concentration evolution of physical properties correlation with surface morphology of CdTe thin films for solar cells. *Mater. Res. Bull.* **2018**, *97*, 128–135. [[CrossRef](#)]
7. Szeles, C. CdZnTe and CdTe materials for X-ray and gamma ray radiation detector applications. *Phys. Status Solidi B* **2004**, *241*, 783–790. [[CrossRef](#)]
8. Richter, M.; Siffert, P. High resolution gamma ray spectroscopy with CdTe detector systems. *Nucl. Instrum. Methods Phys. Res. A* **1992**, *322*, 529–537. [[CrossRef](#)]
9. Schlesinger, T.; Toney, J.; Yoon, H.; Lee, E.; Brunett, B.; Franks, L.; James, R. Cadmium zinc telluride and its use as a nuclear radiation detector material. *Mater. Sci. Eng. R: Rep.* **2001**, *32*, 103–189. [[CrossRef](#)]
10. Scheiber, C.; Giakosb, G.C. Medical applications of CdTe and CdZnTe detectors. *Nucl. Instrum. Methods Phys. Res. A* **2001**, *458*, 12–25. [[CrossRef](#)]
11. Sordo, S.D. Progress in the development of CdTe and CdZnTe semiconductor radiation detectors for astrophysical and medical applications. *Sensors* **2009**, *9*, 3491–3526. [[CrossRef](#)] [[PubMed](#)]
12. Thomas, B.; Veale, M.; Wilson, M.; Seller, P.; Schneider, A.; Iniewski, K. Characterisation of Redlen high-flux CdZnTe. *J. Instrum.* **2017**, *12*, C12045. [[CrossRef](#)]
13. Prokesch, M.; Soldner, S.A.; Sundaram, A.G. CdZnTe detectors for gamma spectroscopy and x-ray photon counting at 250×10^6 photons/(mm² s). *J. Appl. Phys.* **2018**, *124*, 044503. [[CrossRef](#)]
14. Rudolph, P.; Mühlberg, M. Basic problems of vertical Bridgman growth of CdTe. *Mater. Sci. Eng. B* **1993**, *16*, 8–16. [[CrossRef](#)]
15. Feigelson, R.S.; Route, R.R. *Improved Techniques for the Growth of High Quality Cadmium Telluride Crystals*; Center for Materials Research, Stanford University: Singapore, 1985.
16. Carcelén, V. New approaches in order to enlarge the grain size of bulk CdZnTe (CZT) crystals. *J. Optoelectron. Adv. Mater.* **2008**, *10*, 3135–3140.
17. Hossain, A.; Bolotnikov, A.; Camarda, G.; Cui, Y.; Gul, R.; Roy, U.; Yang, G.; James, R. Direct observation of influence of secondary-phase defects on CZT detector response. *J. Cryst. Growth* **2017**, *470*, 99–103. [[CrossRef](#)]
18. Schulz-DuBois, E.O.; Scheel, H.J. Flux growth of large crystals by the accelerated crucible rotation technique. *J. Cryst. Growth* **1971**, *8*, 304–306.
19. Schulz-Dubois, E. Accelerated crucible rotation: Hydrodynamics and stirring effect. *J. Cryst. Growth* **1972**, *12*, 81–87. [[CrossRef](#)]
20. Scheel, H. Accelerated crucible rotation: A novel stirring technique in high-temperature solution growth. *J. Cryst. Growth* **1972**, *13–14*, 560–565. [[CrossRef](#)]
21. Datta, A.; Swain, S.; Cui, Y.; Burger, A.; Lynn, K. Correlations of Bridgman-Grown Cd_{0.9}Zn_{0.1}Te Properties with Different Ampoule Rotation Schemes. *J. Electron. Mater.* **2013**, *42*, 3041–3053. [[CrossRef](#)]
22. Roy, U.N.; Weiller, S.; Stein, J.; Gueorguiev, A. Unseeded growth of CdZnTe:In by THM technique. *Proc. SPIE* **2009**, *7449*, 74490U.
23. Bolotnikov, A.E.; Abdul-Jabbar, N.M.; Babalola, O.S.; Camarda, G.S.; Cui, Y.; Hossain, A.M.; Jackson, E.M.; Jackson, H.C.; James, J.A.; Kohman, K.T.; et al. Effects of Te Inclusions on the Performance of CdZnTe Radiation Detectors. *IEEE Trans. Nucl. Sci.* **2008**, *55*, 2757–2764. [[CrossRef](#)]
24. Rudolph, P.; Koh, H.; Schäfer, N.; Fukuda, T. The crystal perfection depends on the superheating of the mother phase too—Experimental facts and speculations on the “melt structure” of semiconductor compounds. *J. Cryst. Growth* **1996**, *166*, 578–582. [[CrossRef](#)]
25. Chu, M.; Terterian, S.; Ting, D.; Wang, C.C.; Benson, J.D.; Dinan, J.H.; James, R.B.; Burger, A. Effects of excess tellurium on the properties of CdZnTe radiation detectors. *J. Electron. Mater.* **2003**, *32*, 778–782. [[CrossRef](#)]
26. Chu, M.; T, S.; Ting, D.; James, R.B.; Szawlowski, M.; Visserc, G.J. Effects of p/n Inhomogeneity on CdZnTe Radiation Detectors. In Proceedings of the SPIE Photonics West, San Jose, CA, USA, 25–31 January 2003.
27. Zhang, X.; Zhao, Z.; Zhang, P.; Ji, R.; Li, Q. Comparison of CdZnTe crystals grown by the Bridgman method under Te-rich and Te-stoichiometric conditions and the annealing effects. *J. Cryst. Growth* **2009**, *311*, 286–291. [[CrossRef](#)]
28. Suzuki, K.; Seto, S.; Sawada, T.; Imai, K. Carrier transport properties of HPB CdZnTe and THM CdTe:Cl. *IEEE Trans. Nucl. Sci.* **2002**, *49*, 1287–1291. [[CrossRef](#)]
29. Stadler, W.; Hofmann, D.M.; Alt, H.C.; Muschik, T.; Meyer, B.K.; Weigel, E.; Müller-Vogt, G.; Salk, M.; Rupp, E.; Benz, K.W. Optical investigations of defects in Cd_{1-x}Zn_xTe. *Phys. Rev. B* **1995**, *51*, 10619. [[CrossRef](#)]

30. Gul, R.; Bolotnikov, A.; Kim, H.K.; Rodriguez, R.; Keeter, K.; Li, Z.; Gu, G.; James, R.B. Point Defects in CdZnTe Crystals Grown by Different Techniques. *J. Electron. Mater.* **2011**, *40*, 274–279. [[CrossRef](#)]
31. Rudolph, P. Non-stoichiometry related defects at the melt growth of semiconductor compound crystals—A review. *Cryst. Res. Technol.* **2003**, *38*, 542–554. [[CrossRef](#)]
32. Greenberg, J.H. *Thermodynamic Basis of Crystal Growth: PTX Phase Equilibrium and Non-Stoichiometry*; Springer Science & Business Media: New York, NY, USA, 2013; Volume 44.
33. McCoy, J.J.; Kakkireni, S.; Gélinas, G.; Garaffa, J.F.; Swain, S.K.; Lynn, K.G. Effects of excess Te on flux inclusion formation in the growth of cadmium zinc telluride when forced melt convection is applied. *J. Cryst. Growth* **2020**, *535*, 125542. [[CrossRef](#)]
34. Bolotnikov, A.E.; Camarda, G.S.; Carini, G.A.; Cui, Y.; Li, L.; James, R.B. Modeling the geometrical effects of Te precipitates on electron transport in CdZnTe. *Nucl. Instrum. Methods Phys. Res. A* **2007**, *571*, 125. [[CrossRef](#)]
35. Bolotnikov, A.E.; Camarda, G.S.; Carini, G.A.; Cui, Y.; Kohman, K.T.; Li, L.; Salomon, M.B.; James, R.B. Performance-limiting defects in CdZnTe detectors. *IEEE Trans. Nucl. Sci.* **2007**, *54*, 821–827. [[CrossRef](#)]
36. Carini, G.A.; Bolotnikov, A.E.; Camarda, G.S.; Wright, G.W.; Li, L.; James, R.B. Effect of Te precipitates on the performance of CdZnTe detectors. *Appl. Phys. Lett.* **2006**, *88*, 143515. [[CrossRef](#)]
37. Kim, K.H.; Bolotnikov, A.E.; Camarda, G.S.; Hossain, A.; Gul, R.; Yang, G.; Cui, Y.; Prochazka, J.; Franc, J.; Hong, J.; et al. Defect levels of semi-insulating CdMnTe:In crystals. *J. Appl. Phys.* **2011**, *109*, 113715–113720. [[CrossRef](#)]
38. Grill, R.; Franc, J.; Belas, E.; Höschl, P.; Nahlovskyy, B.; Moravec, P.; Fochuk, P.; Verzhak, Y.; Panchuk, O. Dynamics of Point Defects in Tellurium-Rich CdTe. *IEEE Trans. Nucl. Sci.* **2007**, *54*, 792–797. [[CrossRef](#)]
39. Lindström, A.; Klintonberg, M.; Sanyal, B.; Mirbt, S. Cl-doping of Te-rich CdTe: Complex formation, self-compensation and self-purification from first principles. *AIP Adv.* **2015**, *5*, 087101. [[CrossRef](#)]
40. Yu, P.; Jie, W. Effects of post-growth annealing on the performance of CdZnTe:In radiation detectors with different thickness. *Nucl. Instrum. Methods Phys. Res. A* **2014**, *737*, 29–32. [[CrossRef](#)]
41. Yang, G.; Bolotnikov, A.E.; Fochuk, P.M.; Cui, Y.; Camarda, G.S.; Hossain, A.; Kim, K.H.; Horace, J.; McCall, B.; Gul, R.; et al. Effects of thermal annealing on the structural properties of CdZnTe crystals. In Proceedings of the Hard X-Ray, Gamma-Ray, and Neutron Detector Physics XIII, San Diego, CA, USA, 21 August 2011; Volume 8142, p. 814217. [[CrossRef](#)]
42. Fochuk, P.; Grill, R.; Nakonechnyi, I.; Kopach, O.; Panchuk, O.; Verzhak, Y.; Belas, A.E.B.E.; Yang, G.; James, R.B. Effect of Cd_{0.9}Zn_{0.1}Te:In Crystals Annealing on Their High-Temperature Electrical Properties. *IEEE Trans. Nucl. Sci.* **2011**, *58*, 2346–2351. [[CrossRef](#)]
43. Bugar, M.; Belas, E.; Grill, R.; Prochazka, J. Inclusions Elimination and Resistivity Restoration of CdTe:Cl Crystals by Two-Step Annealing. *IEEE Trans. Nucl. Sci.* **2011**, *58*, 1942–1948. [[CrossRef](#)]
44. Yu, P.; Jie, W.; Wang, T. Detector-grade CdZnTe:In crystals obtained by annealing. *J. Electron. Mater.* **2011**, *46*, 3749–3752. [[CrossRef](#)]
45. Yang, G.; Bolotnikov, A.; Fochuk, P.; Kopach, O.; Franc, J.; Belas, E.; Kim, K.; Camarda, G.; Hossain, A.; Cui, Y.; et al. Post-growth thermal annealing study of CdZnTe for developing room-temperature X-ray and gamma-ray detectors. *J. Cryst. Growth* **2012**, *379*, 16–20. [[CrossRef](#)]
46. Hofmann, D.M.; Stadler, W.; Christmann, P.; Meyer, B.K. Defects in CdTe and Cd_{1-x}Zn_xTe. *Nucl. Instr. and Meth. Phys. Res.* **1996**, *A380*, 117–120. [[CrossRef](#)]
47. Höschl, P.; Grill, R.; Franc, J.; Moravec, P.; Belas, E. Native defect equilibrium in semi-insulating CdTe(Cl). *Mater. Sci. Eng. B* **1993**, *16*, 215. [[CrossRef](#)]
48. Popovych, V.; Virt, I.; Sizov, F.; Tetyorkin, V.; Tsybrii, Z.T.; Darchuk, L.; Parfenjuk, O.; Ilashchuk, M. The effect of chlorine doping concentration on the quality of CdTe single crystals grown by the modified physical vapor transport method. *J. Cryst. Growth* **2007**, *308*, 63–70. [[CrossRef](#)]
49. Malm, H.L.; Martini, M. Polarization Phenomena in CdTe Nuclear Radiation Detectors. *IEEE Trans. Nucl. Sci.* **1974**, *21*, 322–330. [[CrossRef](#)]